Oxidation behavior of Si$_3$N$_4$-TiN composites at 1400 ºC

T. S. Ferreira[a], F. M. S. Carvalho[b], C. C. Guedes-Silva[a]* ⓘ

[a]Instituto de Pesquisas Energéticas e Nucleares, Comissão Nacional de Energia Nuclear, Av. Prof. Lineu Prestes, 2242, 05508-000, São Paulo, SP, Brasil.
[b]Universidade de São Paulo, Instituto de Geociências, 05508-080, São Paulo, SP, Brasil.

In this paper, the oxidation behavior of silicon nitride with different contents of TiN was evaluated at 1400 ºC for 64 hours in air. The oxidized samples were characterized by X-ray diffraction, scanning electron microscopy and energy dispersive X-ray spectroscopy. Weight gain measurements have shown that the oxidation followed a multiple-law model with linear, parabolic, and logarithmic contributions. The samples presented high weight gain at the beginning of the process followed by the formation of an amorphous silica surface layer containing Y$_2$Ti$_2$O$_7$ and rutile crystals. Cracks and holes were detected on the oxide layer. The oxidation resistance of the composites was strongly influenced by the initial content of TiN.

Keywords: *silicon nitride, titanium nitride, oxidation, microstructure.*

1. Introduction

Silicon nitride ceramics are widely used in structural applications owing to their low thermal expansion, high strength, hardness, and corrosion resistance[1,2]. However, the fragile behavior of this material, which can reduce the lifetime of the components, has led researchers to investigate alternatives for obtaining silicon nitride ceramics with high strength and fracture toughness. One of them is related to the development of silicon nitride composites containing a second reinforced phase, such as fibers, whiskers or particles to induce fracture toughness mechanisms[3-6].

Although many different composites have been studied, those with a conductive phase are more attractive since they can improve the mechanical properties and machinability of the sintered components by electrical discharge machining (EDM). In this context, TiN as a second phase in silicon nitride ceramics has been highlighted in the last years, mainly because of its high electrical conductivity, hardness and strength. Moreover, the thermal expansion coefficient of TiN higher than that of Si$_3$N$_4$ tends to induce the formation of tensile and compressive stress around the TiN particles which improves the fracture toughness of the composite[5,7-9].

Si$_3$N$_4$-TiN composites are employed in many high-temperature applications, such as heat exchangers, crucibles for molten metal, turbine and automotive engine components, and cutting tools[10-13]. On the other hand, Si$_3$N$_4$-TiN composites exhibit lower oxidation than pure silicon nitride ceramics. The process just starts at around 600 ºC, due to the oxidation of TiN[14], which is governed by a second-order reaction. As the temperature increases, many diffusional mechanisms take place simultaneously, becoming the oxidation more complex. Deschaux-Beaume et al.[15,16] studying the oxidation of Si$_3$N$_4$-TiN composites between 1000–1200 ºC observed that the process occurred in three steps. The first step was characterized by the oxidation of Si$_3$N$_4$ and TiN into SiO$_2$ and TiO$_2$ phases, respectively. In the second step, the oxygen diffusion through TiO$_2$ and SiO$_2$ already formed was related to controlling the TiN oxidation. In the third step, they associated oxidation of the TiN and Si$_3$N$_4$ to the oxygen diffusion through the silica layer. Moreover, Bracisiewics et al.[17] found oxide scales and a multilayer microstructure under the oxide towards the bulk due to the oxidation of hot pressed Si$_3$N$_4$–35 vol.% TiN in air at 800, 1000 and 1200 ºC for 100 h. In turn, considering oxidation of sintered Si$_3$N$_4$/TiN nanocomposites at 850 and 1150 °C for 50 h, Zou et al.[5] concluded that the oxygen diffusion at 1150 °C toward the matrix accelerated the weight gain of the materials as a consequence of the pore and cracks formed between the oxidizing layer and matrix phase.

Another factor with a great role in the oxidation of Si$_3$N$_4$-TiN composites is the intergranular phase present in the grain boundary. For Feldhoff et al.[18] this process is strongly dependent on the glass transition temperature of the intergranular glass since this phase affects the species dissolution and diffusional transport. According to Bracisiewicz et al.[17] and Bellosi et al.[19], sintering aid cations in the intergranular phase tend to diffuse from the bulk to the reaction interface, forming glassy silicates and other oxidation products. Moreover, the crystallization of SiO$_2$ in cristobalite becomes the oxidation process even more complex.

In this paper, Si$_3$N$_4$-TiN composites with 5 to 30 wt.% TiN were exposed at 1400 ºC for 64 hours in air to evaluate the oxidation behavior and the morphology of the formed oxide layer. The tests temperature was selected considering the limited number of oxidation studies of Si$_3$N$_4$-TiN composites in such condition and their potential to be used in applications at temperatures as high as 1400 C, as in turbine blade[12] and space technology[20].

*e-mail: cecilia.guedes@ipen.br

2. Experimental Materials

α-Si_3N_4 powders (UBE, SN-E10), TiN powders (H.C. Starck), Al_2O_3 (CT 3000SG, Almatis) and Y_2O_3 (Sigma Aldrich) were used as raw materials. As shown in Table 1, four compositions of powders with $90Si_3N_4$-$5Y_2O_3$-$5Al_2O_3$ (in wt.%), coded as SNYA, and TiN were mixed by ball milling using Al_2O_3 balls for 24 h in isopropanol and then dried using a rotary evaporator. The powders were uniaxially pressed at 50 MPa into cylindrical pellets (12×20 mm) followed by cold isostatic pressing at 250 MPa. The green bodies were then placed in a graphite crucible in a powder bed and sintered using a graphite resistance furnace (Thermal Technology) at 1750 °C under a nitrogen atmosphere.

For the oxidation tests, the sintered samples were rectified in a diamond wheel and cleaned using acetone in an ultrasonic bath. After that, the specimens were placed in an alumina crucible with minimal contact area and inserted in a tubular furnace under air atmosphere at 1400 °C for 64 h. Every weight was measured after 1, 2, 4, 8, 16, 32 and 64 h of exposure while the microstructural characterization of the samples surface was carried out by scanning electron microscopy (SEM, Philips XL-30), energy dispersive X-ray spectroscopy (EDS, JEOL JSM6701F). One specimen of each composition mounted in epoxy resin was cut to observe the cross-section and the oxide layer thickness by SEM/EDS which was estimated using ImageJ[21] as image analysis software. The oxidized surfaces also were analyzed by X-ray diffraction (XRD) using a Bruker D8 Advance X-ray diffractometer (Cu Kα radiation source operated at 40 kV and 40μÅ) in a range from 5 to 90º (2θ) with step of 0.02º (2θ) and 5s/pass. To do that, the pellets were previously fixed onto sample holders with modeling clay and then slightly pressed to adjust their height. To estimate the amount of crystalline phases, we used the RIR method[22], while the amount of amorphous phase was estimated through the peak areas of the amorphous and crystalline phases. The software used for data acquisition and evaluation was Bruker including the PDF-2 database[23].

3. Results

Figure 1 shows the oxidation kinetic of Si_3N_4–TiN composites at 1400 °C. At the beginning of the process,

the samples presented an increased weight gain which was more significantly for those ceramics with higher content of TiN. The influence of TiN on the oxidation behavior is also observed during the entire process since the overall weight gain was greater for SNTN-30, SNTN-20, SNTN-10 and SNTN-5 samples, respectively. This behavior can be attributed to the greater Ti affinity for oxygen than Si, which favors the oxidation of TiN, according to the reaction[17]:

$$TiN + O_2 \rightarrow TiO_2 + \tfrac{1}{2} N_2 \tag{1}$$

In addition, the shape of the curves in Figure 1 is similar. They were fitted by the multiple-law model proposed by Nickel[24] (Equation 2) since the oxidation kinetics could not be described by a simple linear or parabolic law.

$$\frac{\Delta m}{A} = k_l t + k_p \sqrt{t} + k_{log} \log(t) \tag{2}$$

Where $\frac{\Delta m}{A}$ corresponds to the mass change as a function of time (t) and k_l, k_p and k_{log} are linear, parabolic and logarithmic rate constants, respectively.

Table 2 summarizes the kinetic parameters (k_l, k_p and k_{log}) and fit goodness values (R^2) for the fitted curves. While the parabolic term is related to the oxide formation on the samples' surfaces, the linear parameter is negative due to the evaporation of species from the oxide scale, and the logarithmic term can be attributed to crystallization processes[24,25]. Although each rate constant has a physical meaning, there is interaction between the phenomena which also interfered with the constants values of each studied composition.

Table 1. Studied compositions.

Designation	Composition
SNTN-5	SNYA+5 wt.% TiN
SNTN-10	SNYA+10 wt.% TiN
SNTN-20	SNYA+20 wt.% TiN
SNTN-30	SNYA+30 wt.% TiN
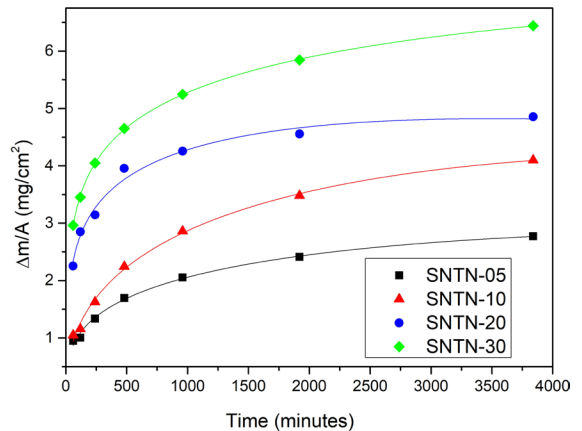
Figure 1. Plots of weight gain versus exposure time of the Si_3N_4–TiN at 1400 °C in air.

Table 2. Linear, parabolic and logarithmic contributions, and R^2 (fit goodness) values obtained from fitted oxidation curves.

Sample	k_l (mg.cm^{-2}.min^{-1})	k_p (mg.cm^{-2}.min$^{-1/2}$)	k_{log} (mg.cm^{-2})	R^2
SNTN-05	-3.117x10^{-4}	0.047	0.128	0.992
SNTN-10	-6.742x10^{-4}	0.101	0.048	0.995
SNTN-20	-5.034x10^{-4}	0.043	0.497	0.980
SNTN-30	-1.801x10^{-4}	0.251	0.675	0.999
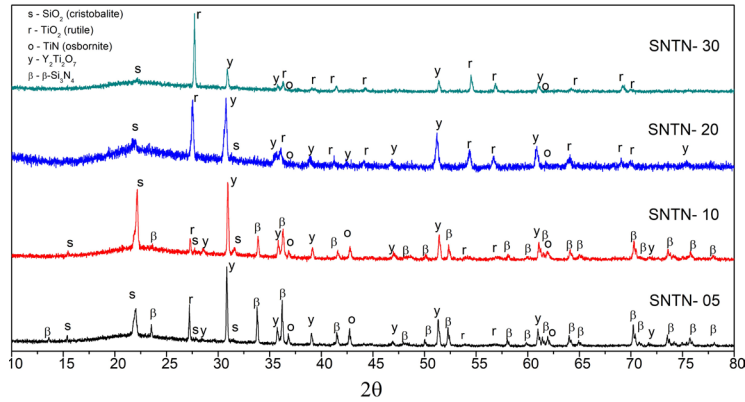
Figure 2. XRD spectra of oxidized Si_3N_4-TiN samples after 64 h at 1400 °C.

XRD patterns of the oxidized samples are shown in Figure 2. The presence of rutile (TiO_2) confirms that the reaction described in Equation 1 occurred on the surface of all samples. Cristobalite (SiO_2) and an amorphous phase with a broad band between 15º and 30º, characteristic of amorphous silica were also detected. These results are attributed to the Si_3N_4 oxidation which tends to form SiO_2 which reacts with yttrium and aluminum cations from the amorphous intergranular phase of the sintered composites. The formation of amorphous silica tends to create a protective coating on the samples' surfaces, avoiding the diffusion of oxygen and reducing the oxidation rate of the composite. Moreover, the cristobalite is a consequence of the partial crystallization of the amorphous silica contributing to the logarithmic term in Equation 2.

The diffractograms in Figure 2 also show that the Y^{3+} ions, diffused from the intergranular phase of composites, reacted with TiO_2 formed during the oxidation process forming yttrium titanate ($Y_2Ti_2O_7$) during the tests. The presence of osbornite (TiN) and β-Si_3N_4 was also detected confirming the microstructure of the samples was preserved.

By XRD semi-quantitative analysis (Figure 3), we can observe that the prevalent phases on the surface of all samples are $Y_2Ti_2O_7$ and the amorphous phase. Moreover, the amount of Si_3N_4 and TiN on the oxidized surfaces tended to be decreased for samples with higher content of TiN in the initial composition, while the amount of TiO_2 was increased and that of cristobalite was found to be almost constant. These results are in good agreement with those of weight gain in Figure 1, demonstrating that the oxidation resistance of the composites is directly related to the reaction shown in Equation 1.

Figure 4 illustrates SEM-backscatter images of polished cross-sections of the oxidized samples with EDS maps for O, Si, and Ti. The Y and Al distributions could not be analyzed, as the low concentration of these elements in the samples did not make it possible to differentiate their peaks from the background. In general, the cross sections are formed by three areas, characterized by (i) the bulk, (ii) a sub-layer and (iii) an external layer. Although all analyzed elements are present in the entire area, the surface is formed by a grey phase containing silicon and oxygen, with Ti-rich crystals that appear in the SEM images as white structures. The sub-layer is extremely porous and formed basically by silicon
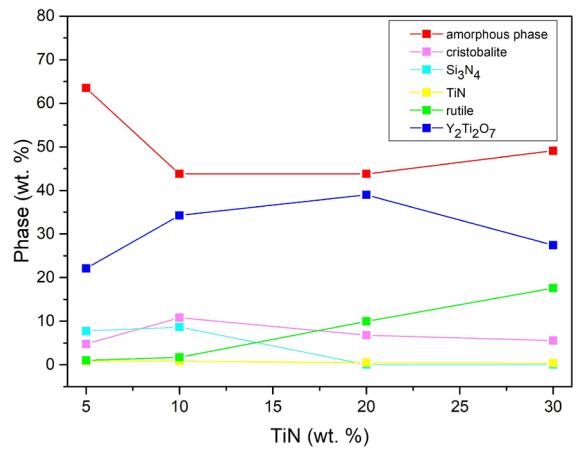
Figure 3. Evolution of the phases on the oxidized sample's surface with the content of TiN.

Table 3. Oxide layer thickness on the samples oxidized at 1400ºC for 64 hours.

Sample	Thickness (µm)
SNTN-5	85.78 ± 10.70
SNTN-10	78.81 ± 16.62
SNTN-20	153.28 ± 24.30
SNTN-30	285.26 ± 31.44

and oxygen, while the bulk has titanium and silicon, as the main elements. Associating with XRD results, the external layer is probably the amorphous phase and/or cristobalite with $Y_2Ti_2O_7$ and/or TiO_2 crystals, as identified in Figure 2. Moreover, the sub-layer must be formed by cristobalite or amorphous phase, and the bulk is Si_3N_4 and TiN, suggesting that the inner region of the composite remained well kept up. Besides the porosity and number of Ti-rich crystals on the surfaces, the oxidized layer thickness tended to increase with the initial content of TiN on the samples, as shown in Table 3.

These results are in line with those found by Bracisiewicz et al.[17] in their study about the oxidation of Si_3N_4-TiN composites up to 1200 °C. In such work, the

authors also identified a porous sub-layer rich in titania and silica, attributed to the titanium diffusion toward the surface. For them, with the porous sub-layer formation, the migration of titanium cations became limited which led to the oxidation process being controlled by oxygen diffusion through TiO_2 and porosity. In addition, oxidation of Si_3N_4 formed a silica glassy phase, which filled the porosity in the TiO_2 sub-layer formed. After that, oxidation of both TiN and Si_3N_4 phases is controlled by oxygen diffusion through the silica sub-layer[16].

Figure 5 shows a backscattered electron image of a detailed area from the external layer of SNTN-20 coded sample. The points where EDS analysis was performed (Table 4) are also indicated. From the different contrasts produced by the difference between the atomic numbers of elements, it is possible to observe the presence of three phases characterized by grey crystals (Points 1 to 3), white crystals (Points 4 to 6) and the matrix (Points 7 and 8). Combining diffractograms in Figure 2 with the EDS semi-quantitative results in Table 4, probably the grey crystals (Points 1 to 3) correspond to rutile, while the white crystals are $Y_2Ti_2O_7$, and the matrix is cristobalite and an amorphous phase containing Si, Al, Ti, and O. Aluminum cations in the amorphous phase come from the intergranular phase of the sintered composites. Before the oxidation tests, aluminum cations are present in the intergranular phase of Si_3N_4-TiN composites as a result

of cooling of the liquid phase during the sintering process due to the reaction between the additives (Al_2O_3 and Y_2O_3) with silica (SiO_2) on the surface of the Si_3N_4 particles, as described in our previous work[26].

The surface morphology backscattered electron images of the samples after oxidation are shown in Figure 6. The oxidized surface of all samples is formed by a grey matrix besides grey and white crystals also observed in Figure 5. However, the greater the amount of TiN in the initial compositions, the greater the number of crystals on the layer. Since the XRD semi-quantitative analysis (Figure 3) shows that the amount of rutile increased with the initial content of TiN, we can associate the increased number of crystals to the greater formation of rutile. As well as this, it is possible to notice many holes due to bubbles produced by gaseous products (such as N_2 and SiO) released during the oxidation process. The volatilization of these species leads to mass loss justifying the negative linear terms in Table 2.

Cracks are also present on the oxide layer. They were probably initiated during the cooling after oxidation, as a result of tensile stresses created by a volume contraction due to the transformation of the high-temperature cristobalite phase to the low-temperature cristobalite phase[27]. Both holes and cracks contributed to decline the oxidation resistance since they favor the oxygen diffusion through the formed oxide layer to the bulk of the material[28].
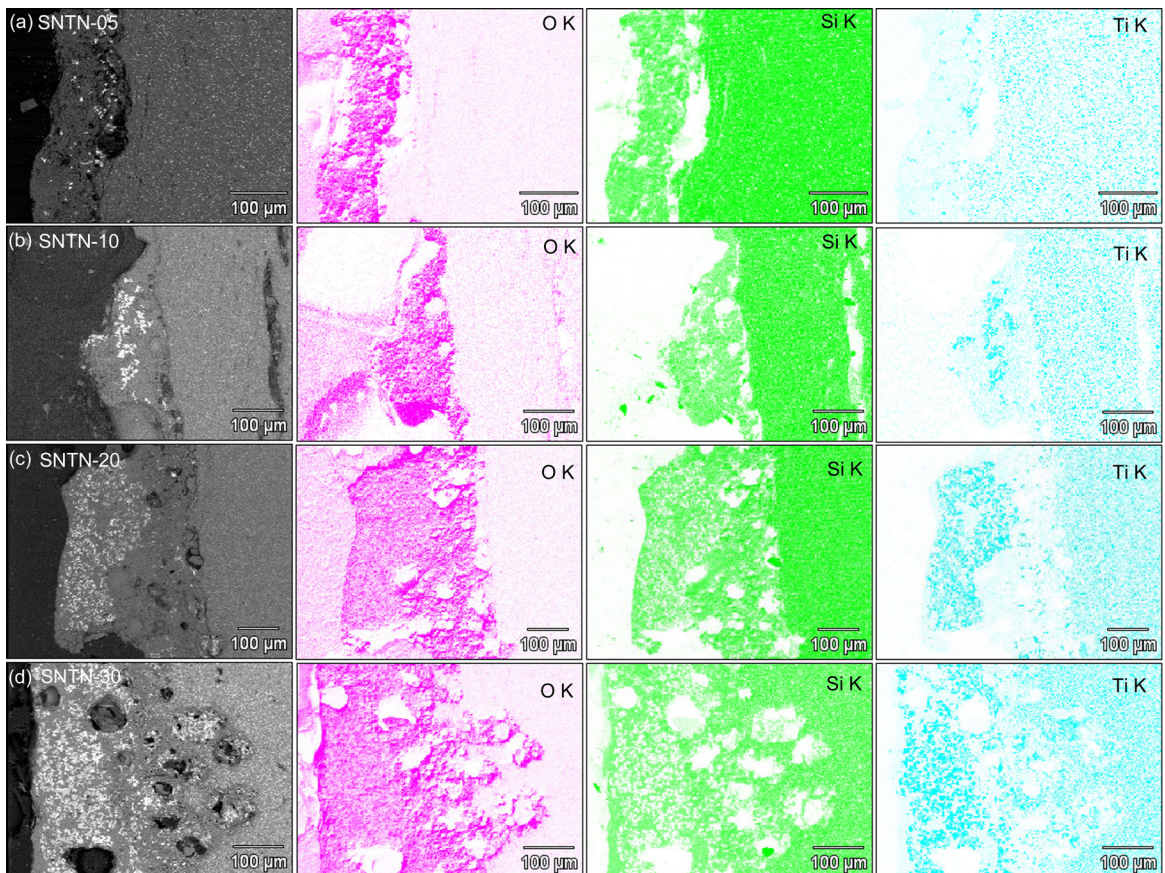
Figure 4. SEM images of cross-sectional oxidized samples and corresponding X-ray maps of oxygen, silicon, and titanium obtained by EDS.

Table 4. Content of elements from Point 1 to Point 8 (at.%) of Figure 5.

	N-K	O-K	Na-K	Al-K	Si-K	Ti-K	Y-L
Point 1		48.1		0.1	0.2	51.6	
Point 2		46.6		0.2	0.3	53.0	
Point 3	4.9	44.8		0.2	0.6	49.5	
Point 4		44.9		0.3	0.0	31.5	23.4
Point 5		27.2		0.2		45.3	27.3
Point 6		72.1		0.2		15.6	12.1
Point 7		76.4		2.4	19.9	1.3	
Point 8		70.4	1.4	2.9	23.6	1.7	
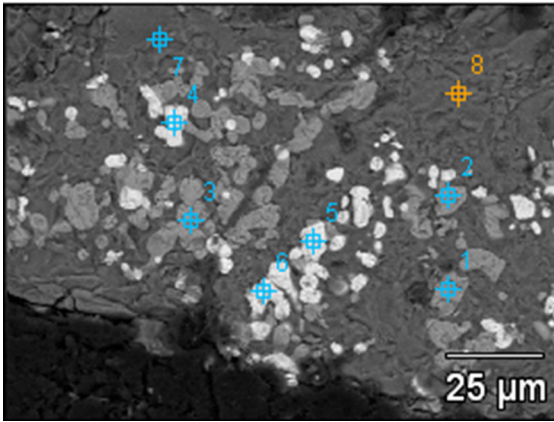
Figure 5. Backscattered electron (BSE) image of the oxidized SNTN-20 sample cross section showing the locations of the EDS analysis points of Table 4.

4. Conclusion

The oxidation behavior of Si_3N_4-TiN composites was investigated at 1400 ℃ for 64 hours in air. The oxidation curves were well fitted by a multiple-law model with linear, parabolic, and logarithmic terms. After 64 hours of exposition in air, it was formed on all samples' surfaces, a protective layer characterized by amorphous silica containing cristobalite, $Y_2Ti_2O_7$, and rutile crystals. Holes and cracks were also presented, contributing to accelerating the oxidation of the samples since they can provide channels for oxygen diffusion.

As a result of the great Ti affinity for oxygen, both weight gain and oxidized layer thickness increased with the initial content of TiN. Hence, although TiN additions may improve the mechanical behavior of silicon nitride ceramics, their concentration must be carefully selected to avoid high reductions in oxidation resistance of the final sintered composites.
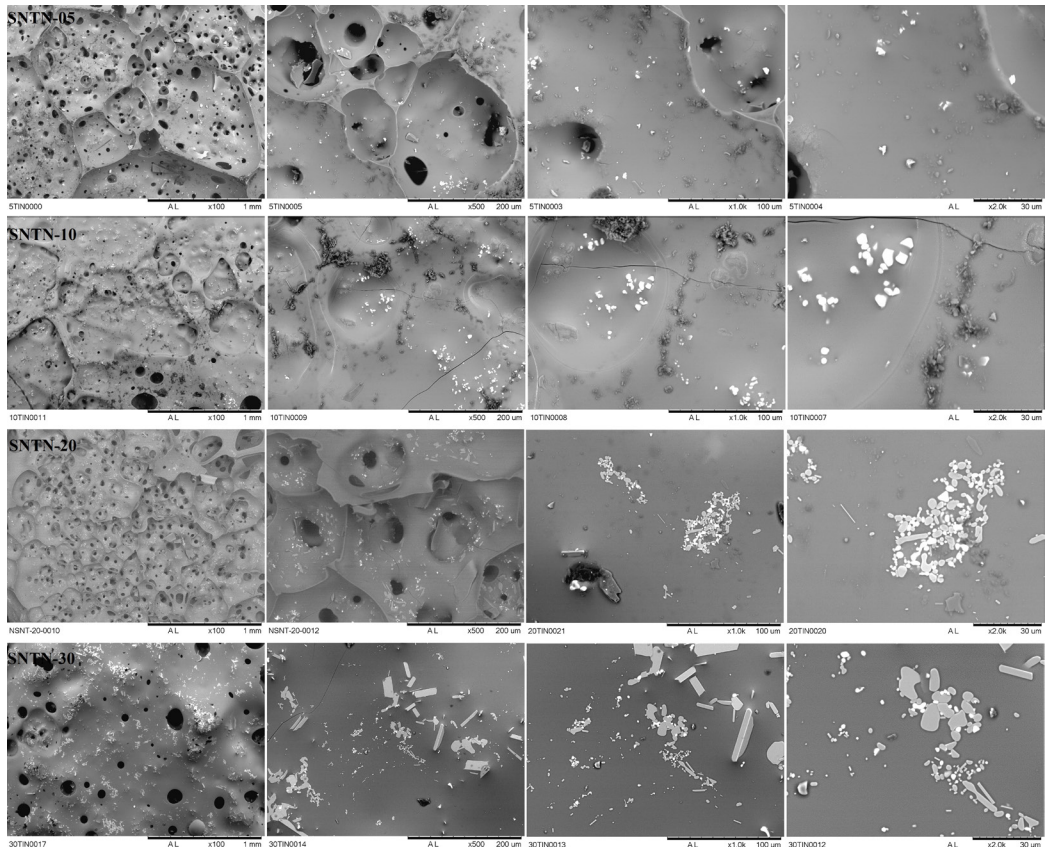
Figure 6. Backscattered electron (BSE) images of the external layer of oxidized samples at different magnifications.

5. Acknowledgments

6. References

1. Anbuchezhiyan G, Mohan B, Senthilkumar N, Pugazhenthi R. Synthesis and characterization of silicon nitride reinforced Al–Mg–Zn alloy composites. Met Mater Int. 2021;27(8):3058-69. http://dx.doi.org/10.1007/s12540-020-00906-3.

2. Perevislov SN. Sintering behavior and properties of reaction-bonded silicon nitride. Russ J Appl Chem. 2021;94(2):143-51. http://dx.doi.org/10.1134/S1070427221020038.

3. Gogotsi YG. Particulate silicon nitride-based composites. J Mater Sci. 1994;29(10):2541-56. http://dx.doi.org/10.1007/BF00356803.

4. Gao L, Jin X, Li J, Li Y, Sun J. BN/Si_3N_4 nanocomposite with high strength and good machinability. Mater Sci Eng A. 2006;415(1-2):145-8. http://dx.doi.org/10.1016/j.msea.2005.09.085.

5. Zou B, Huang CZ, Liu HL, Chen M. Preparation and characterization of Si_3N_4/TiN nanocomposites ceramic tool materials. J Mater Process Technol. 2009;209(9):4595-600. http://dx.doi.org/10.1016/j.jmatprotec.2008.10.025.

6. Kovalčíková A, Balazsi C, Dusza J, Tapasztó O. Tapasztó O. Mechanical properties and electrical conductivity in a carbon nanotube reinforced silicon nitride composite. Ceram Int. 2012;38(1):527-33. http://dx.doi.org/10.1016/j.ceramint.2011.07.038.

7. Ahmad N, Obara K, Sameshima S, Sueyoshi H. Characterization of Si_3N_4-TiN composites prepared by Spark Plasma Sintering. Trans Mater Res Soc Jpn. 2009;34(4):793-7. http://dx.doi.org/10.14723/tmrsj.34.793.

8. Zhou M, Zhong J, Zhao J, Rodrigo D, Cheng YB. Microstructures and properties of Si_3N_4/TiN composites sintered by hot pressing and spark plasma sintering. Mater Res Bull. 2013;48(5):1927-33. http://dx.doi.org/10.1016/j.materresbull.2013.01.045.

9. Srinivasan VP, Palani PK. Surface integrity, fatigue performance and dry sliding wear behaviour of Si_3N_4–TiN after wire-electro discharge machining. Ceram Int. 2020;46(8):10734-9. http://dx.doi.org/10.1016/j.ceramint.2020.01.082.

10. Selvarajan L, Venkataramanan K. Surface morphology and drilled hole accuracy of conductive ceramic composites Si_3N_4–TiN and $MoSi_2$–SiC on EDMed surfaces. Wear. 2023;530-531:204973. http://dx.doi.org/10.1016/j.wear.2023.204973.

11. Murugan C, Kumar RMS, Alagarsamy SV. Investigations on electric discharge machining behaviour of Si_3N_4-TiN ceramic composite. Silicon. 2022;14(2):547-55. http://dx.doi.org/10.1007/s12633-020-00848-w.

12. Selvarajan L, Rajavel R, Prakash B, Mohan DG, Gopi S. Investigation on spark electrical discharge machining of Si_3N_4 based advanced conductive ceramic composites. Mater Today Proc. 2020;27:2174-8. http://dx.doi.org/10.1016/j.matpr.2019.09.090.

13. Selvarajan L, Rajavel R, Venkataramanan K, Srinivasan VP. Experimental investigation on surface morphology and recasting layer of Si_3N_4-TiN composites machined by die-sinking and

14. rotary EDM. Ceram Int. 2023;49(5):8487-501. http://dx.doi.org/10.1016/j.ceramint.2022.11.011.

14. Mazerolles L, Feldhoff A, Trichet MF, Backhaus-Ricoult M. Oxidation behavior of Si_3N_4–TiN ceramics under dry and humid air at high temperature. J Eur Ceram Soc. 2005;25(10):1743-8. http://dx.doi.org/10.1016/j.jeurceramsoc.2004.12.016.

15. Deschaux-Beaume F, Fréty N, Cutard T, Colin C. Oxidation modelling of a Si_3N_4–TiN ceramic: microstructure and kinetic laws. Ceram Int. 2007;33(7):1331-9. http://dx.doi.org/10.1016/j.ceramint.2006.04.016.

16. Deschaux-Beaume F, Frety N, Cutard T, Colin C. Oxidation modeling of a Si_3N_4–TiN composite: comparison between experiment and kinetic models. Ceram Int. 2009;35(5):1709-18. http://dx.doi.org/10.1016/j.ceramint.2008.09.006.

17. Bracisiewicz M, Medri V, Bellosi A. Factors inducing degradation of properties after long term oxidation of Si_3N_4–TiN electroconductive composites. Appl Surf Sci. 2002;202(3-4):139-49. http://dx.doi.org/10.1016/S0169-4332(02)00498-1.

18. Feldhoff A, Trichet MF, Mazerolles L, Backhaus-Ricoult M. Electron microscopy study on the high-temperature oxidation of Si_3N_4–TiN ceramics: in situ and ex situ investigations. J Eur Ceram Soc. 2005;25(10):1733-42. http://dx.doi.org/10.1016/j.jeurceramsoc.2004.12.003.

19. Bellosi A, Tampieri A, Liu YZ. Oxidation behaviour of electroconductive Si_3N_4-TiN composites. Mater Sci Eng A. 1990;127(1):115-22. http://dx.doi.org/10.1016/0921-5093(90)90197-B.

20. Vlasova M, Alimbekov MS, Zhelezov PE, Mel'nikov IV, Tokarev VN, Márquez Aguilar PA, et al. Laser-induced Si_3N_4–TiN ceramics degradation. Ceram Int. 2020;46(3):3668-74. http://dx.doi.org/10.1016/j.ceramint.2019.10.087.

21. Rueden CT, Schindelin J, Hiner MC, DeZonia BE, Walter AE, Arena ET, et al. ImageJ2: ImageJ for the next generation of scientific image data. BMC Bioinformatics. 2017;18(1):529. http://dx.doi.org/10.1186/s12859-017-1934-z.

22. Hubbard CR, Evans EH, Smith DK. The reference intensity ratio, I/IC, for computer simulated powder patterns. J Appl Cryst. 1976;9(2):169-74. http://dx.doi.org/10.1107/S0021889876010807.

23. Gates-Rector S, Blanton T. The powder diffraction file: a quality materials characterization database. Powder Diffr. 2019;34(4):352-60. http://dx.doi.org/10.1017/S0885715619000812.

24. Nickel KG. Ceramic matrix composite corrosion models. J Eur Ceram Soc. 2005;25(10):1699-704. http://dx.doi.org/10.1016/j.jeurceramsoc.2004.12.010.

25. Sciti D, Balbo A, Bellosi A. Oxidation behaviour of a pressureless sintered HfB_2–$MoSi_2$ composite. J Eur Ceram Soc. 2009;29(9):1809-15. http://dx.doi.org/10.1016/j.jeurceramsoc.2008.09.018.

26. Ferreira TS, Carvalho FMS, Guedes-Silva CC. Densification and microstructure of Si_3N_4-TiN ceramic composites. Ceramica. 2019;65(Suppl. 1):87-91. http://dx.doi.org/10.1590/0366-6913201965s12605.

27. Qingwei H, Zhihao J. The high temperature oxidation behavior of reaction-bonded silicon carbide. J Mater Process Technol. 2001;110(2):142-5. http://dx.doi.org/10.1016/S0924-0136(00)00859-1.

28. Xie W, Fu Q, Cheng C, Zhang G, Yan N, Wang Z. Effect of La_2O_3 on the oxidation resistance of SiC ceramic at 1973 K: experimental and theoretical study. J Am Ceram Soc. 2020;103(1):614-21. http://dx.doi.org/10.1111/jace.16708.